Supporting Information for "Impact of remineralization profile shape on the air-sea carbon balance"

Jonathan Maitland Lauderdale[1] and B. B. Cael[2]

[1]Department of Earth, Atmospheric and Planetary Sciences, Massachusetts Institute of Technology, Cambridge, MA 02139, USA.

[2]Ocean Biogeochemistry and Ecosystems, National Oceanography Centre, Southampton, SO14 3ZH, UK.

Corresponding authors: JML (jml1@mit.edu) & BBC (cael@noc.ac.uk)

Contents of this file

1. Text "Introduction", "Alternative remineralization profile shapes", and "Supporting simulation results".

2. Figures S1 to S5.

3. Tables S1 to S3.

Introduction

This Supplementary Information contains supporting materials and methods, figures for individual model simulations presented in aggregated form in the main text, as well as tables containing additional globally-aggregated values and anomalies.

Alternative remineralization profile shapes.

Here we outline the derivation and assumptions behind six different remineralization profiles. Assuming timescales of sinking ($\leq$1 month) are shorter than transport by ocean circulation ($\sim$1 year), biological material can be approximated as instantaneously redistributed and remineralized in the vertical.

The most basic curve is a "simple exponential", assuming constant first-order remineralization kinetics and velocity (Banse, 1990; Dutkiewicz et al., 2005; Marsay et al., 2015; Gloege et al., 2017):

$$f_e(z) = C_e e^{-\frac{z}{\ell_e}}, \tag{1}$$

where ℓ_e (meters) is a characteristic lengthscale-the ratio of remineralization timescale and sinking speed.

Including an additional flux of refractory material c to increase the net sinking flux produces the "ballast" model (Armstrong et al., 2001; Gloege et al., 2017):

$$f_b(z) = C_b e^{-\frac{z}{\ell_b}} + c, \tag{2}$$

while explicitly considering the transformation of labile particles (with an initial flux, C_{d1}, and a characteristic lengthscale, ℓ_{d1}) and more refractory material (with an initial flux, C_{d2}, and a characteristic length scale, ℓ_{d2}) results in a "double exponential" profile (Lutz et al., 2002):

$$f_d(z) = C_{d1} e^{-\frac{z}{\ell_{d1}}} + C_{d2} e^{-\frac{z}{\ell_{d2}}}. \tag{3}$$

Relaxing the assumption of constant remineralization timescale, and considering a decrease in the rate of remineralization as labile material is preferentially transformed and refractory material is left behind (as in Eq. 1), leads to a "stretched exponential":

$$f_s(z) = C_s e^{-z^{(1-s)}}, \tag{4}$$

where s is a scale factor between 0–1, for example, if marine particles are degrade similarly to marine sediments, $s \approx 0.95$ (Middelburg, 1989; Cael & Bisson, 2018). A three-parameter stretched exponential with z normalized by z_o is used in many applications. However, fitting z_o and s simultaneously is ill-conditioned, i.e. parameter values are not identifiable, so we have used the simpler two-parameter stretched exponential function, which still provides fits well within global particle flux uncertainty (see Fig. 2).

Second-order degradation kinetics leads to a rational form (Suess, 1980):

$$f_r(z) = \frac{C_r}{z + a} \tag{5}$$

where C_r (meters) is determined by remineralization and sinking while a (meters) is determined by remineralization, sinking, and the initial flux (Cael & Bisson, 2018).

One can model sinking particles as heterogeneous media containing organic carbon, ballast minerals, and heterotrophic bacteria where remineralization slows with time (Rothman & Forney, 2007). This translates to an upper incomplete "gamma" function curve of zeroth order (Cael & Bisson, 2018):

$$f_g(z) = C_g \Gamma\left(0, \frac{z}{\ell_{gmax}}\right), \tag{6}$$

where ℓ_{gmax} (meters) relates to sinking speed and intraparticle bacterial concentration (Rothman & Forney, 2007; Cael & Bisson, 2018). Finally, we note that the "power-law" (Eq. 1) assumes either an increase in sinking speed with depth or a decrease in remineralization rate (Cael & Bisson, 2018). See (Cael & Bisson, 2018) for derivations.

Supporting simulation results:

Fig. S1 shows steady-state zonal averages for the power-law simulations where $b = 0.84 \pm 0.14$. Particulate organic carbon fluxes in the ocean interior increase when the power-law exponent decreases to $b = 0.70$ (Fig. S1a, d) and decrease when the power-law exponent is increased to $b = 0.98$ (Fig. S1c, f). The negative feedback between nutrient availability and biological production of particles can be seen in the surface export flux anomalies (Fig. S1d, f). More efficient export and lower rates of upper ocean remineralization leads to a decrease in recycled nutrient availability, and therefore less overall biological productivity, and lower shallow particulate organic carbon flux when b is reduced (also see globally-integrated community production, ΔB_C, and integrated export fluxes through the deepest annual mixed layer, ΔE_{mld}, values in Table S2). However, reduced shallow export across the deepest mixed layer depth is compensated by lower upper ocean flux attenuation, due to reduced exponent value, resulting instead in enhanced export flux anomalies integrated at 1 km depth. Nutrient availability increases when the remineralization profile is more attenuating in the upper ocean, driving enhanced shallow particulate production and export, but this flux is quickly depleted by the same remineralization profile attenuation, resulting in lower interior ocean export fluxes to the deep ocean.

Biological carbon concentration (C_{bio}) integrates these export fluxes, so that when interior ocean export increases, the deep ocean biological carbon store increases (Fig. S1g), and vice versa (Fig. S1i).

The deep ocean store of biological carbon is directly linked to air-sea carbon partitioning, thus greater ΔC_{bio} indicates uptake of atmospheric carbon by the ocean, and pCO_2 declines. Conversely, when ΔC_{bio} decreases, that carbon outgasses from the ocean causing atmospheric pCO_2 to increase (Table S2).

Fig. S2 shows zonally-averaged anomalies with respect to the reference power-law of export fluxes for the three sets of parameter values and the six different functional forms of remineralization profile. Anomalies largely have an inverse surface-deep ocean contrast, which is captured by the differences in fluxes through the deepest annual mixed layer depth (ΔE_{mld}, Table S3) for the surface ocean changes in particulate export, and fluxes though the 1 km depth horizon (ΔE_{1km}, Table S3) for the deep ocean changes in particulate export. However, the ballast functional form (Eq. S2) has a more complex distribution of particulate flux anomalies in surface, intermediate, and deep waters associated with the additional refractory flux c, which becomes important when the exponentially decaying labile portion of the sinking flux becomes attenuated to low levels.

Fig. S3 shows zonally-averaged anomalies with respect to the reference power-law of the concentration of biological carbon (ΔC_{bio}, Table S3), which integrates the vertical flux and remineralization of particulate organic matter. Again, anomalies largely have an inverse surface-deep ocean contrast, with the deep ocean store of C_{bio} having an inversely proportional relationship with atmospheric CO_2 content (Table S3).

Fig. S4 presents additional relationships between different measures of the change in particulate organic matter export fluxes, and the change in globally-integrated biological carbon reservoir. Conventionally, the deepest mixed layer depth is the threshold between surface ocean, and ocean interior. Once carbon and nutrients are exported below this layer, they are out of the reach of deep winter mixing that would re-expose those waters to the atmosphere on short timescales. However, export out of the surface mixed layer is counterintuitively inversely correlated to the size of the biological carbon reservoir (Fig. S4a). This reflects the strong compensating effect of changes in upper ocean attenuation associated with the different export flux remineralization profiles (see Fig. 3). Even at 1 km there is some scatter between the integrated export flux anomaly and the change in C_{bio} reservoir. Unsurprisingly, this scatter decreases as the export flux horizon becomes deeper (Fig. S4b) and the agreement between sinking carbon fluxes into the deep ocean and deep ocean biological carbon store improves.

References

Armstrong, R. A., Lee, C., Hedges, J. I., Honjo, S., & Wakeham, S. G. (2001). A new, mechanistic model for organic carbon fluxes in the ocean based on the quantitative association of poc with ballast minerals. *Deep Sea Res. Part II*, *49*(1), 219–236. doi: 10.1016/S0967-0645(01)00101-1

Banse, K. (1990). New views on the degradation and disposition of organic particles as collected by sediment traps in the open sea. *Deep Sea Research Part A. Oceanographic Research Papers*, *37*(7), 1177–1195. doi: 10.1016/0198-0149(90)90058-4

Cael, B. B., & Bisson, K. (2018). Particle flux parameterizations: Quantitative and mechanistic similarities and differences. *Front. Mar. Sci.*, *5*, 395. doi: 10.3389/fmars.2018.00395

Dutkiewicz, S., Follows, M. J., & Parekh, P. (2005). Interactions of the iron and phosphorus cycles: A three dimensional model study. *Global Biogeochem. Cycles*, *19*. doi: 10.1029/2004GB002342

Gloege, L., McKinley, G. A., Mouw, C. B., & Ciochetto, A. B. (2017). Global evaluation of particulate organic carbon flux parameterizations and implications for atmospheric pCO_2. *Global Biogeochem. Cycles*, *31*(7), 1192–1215. doi: 10.1002/2016GB005535

Lutz, M., Dunbar, R., & Caldeira, K. (2002). Regional variability in the vertical flux of particulate organic carbon in the ocean interior. *Global Biogeochem. Cycles*, *16*(3), 11-1–11-18. doi: 10.1029/2000GB001383

Marsay, C. M., Sanders, R. J., Henson, S. A., Pabortsava, K., Achterberg, E. P., & Lampitt, R. S. (2015). Attenuation of sinking particulate organic carbon flux through

the mesopelagic ocean. *Proc. Nat. Acad. Sci.*, *112*(4), 1089. doi: 10.1073/pnas.1415311112

Middelburg, J. J. (1989). A simple rate model for organic matter decomposition in marine sediments. *Geochim. Cosmochim. Acta*, *53*(7), 1577–1581. doi: 10.1016/0016-7037(89)90239-1

Rothman, D. H., & Forney, D. C. (2007). Physical model for the decay and preservation of marine organic carbon. *Science*, *316*(5829), 1325. doi: 10.1126/science.1138211

Suess, E. (1980). Particulate organic carbon flux in the oceans—surface productivity and oxygen utilization. *Nature*, *288*(5788), 260–263. doi: 10.1038/288260a0

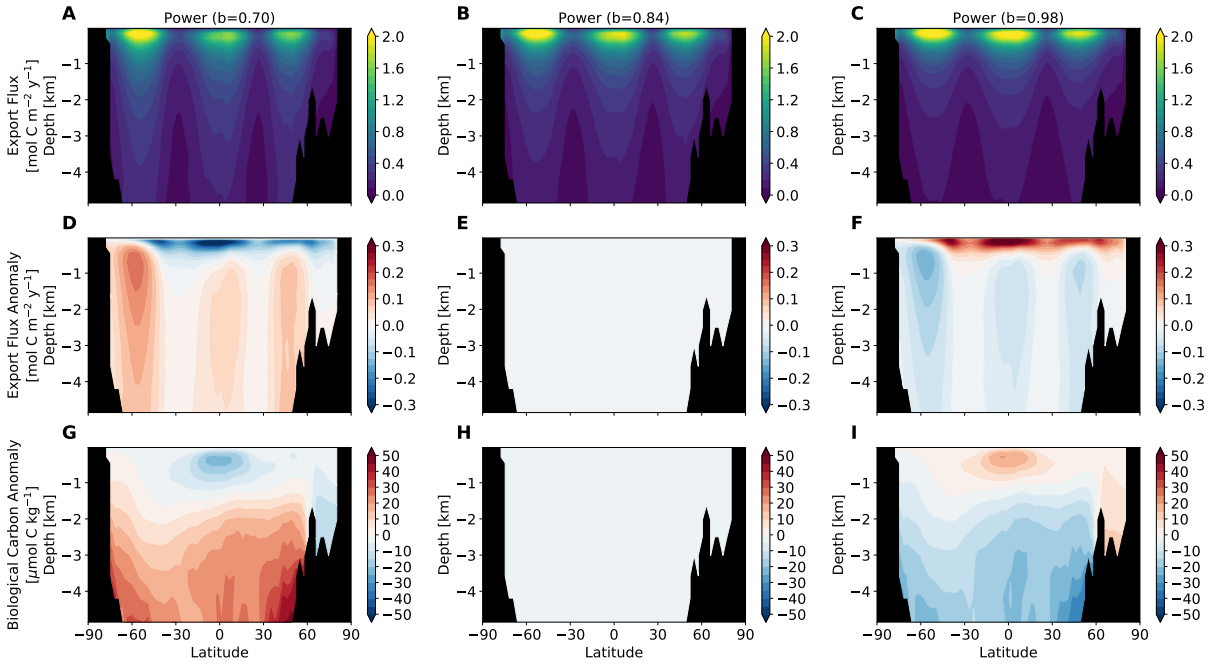

Figure S1. Zonal-average properties for power-law simulations where $b = 0.84 \pm 0.14$ (a–c) particulate organic carbon export fluxes (mol C m^{-2} y^{-1}), (d–f) anomalies of sinking particle export flux compared to the reference power-law simulations (i.e. the middle column, mol C m^{-2} y^{-1}), and similarly (g–h) anomalies of biological carbon concentration (C_{bio}, μmol C kg^{-1}).

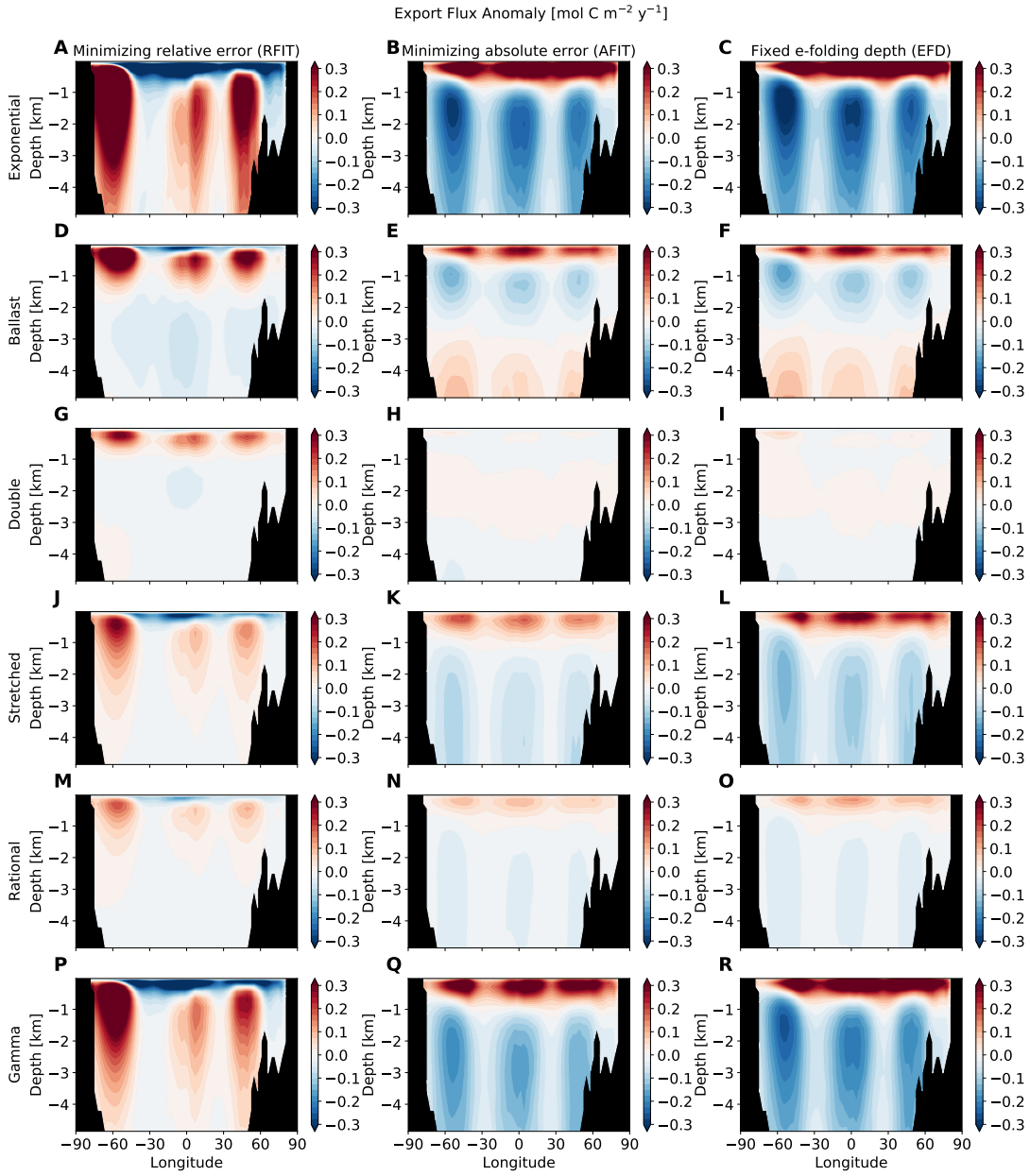

Figure S2. Zonally-averaged export flux anomaly with respect to the reference power-law curve where $b = 0.84$, for the parameter sets where the relative error of the fit is minimized (RFIT, left column), where the absolute error of the fit is minimized (AFIT, middle column), and where the e-folding depth of remineralization is matched to the 164 m of the control curve (EFD, right column), where (a–c) is the simple exponential profile, (d–f) is the ballast profile, (g–i) is the double exponential profile, (j–l) is the stretched exponential profile, (m–o) is the rational profile, and (p–r) is the gamma profile.

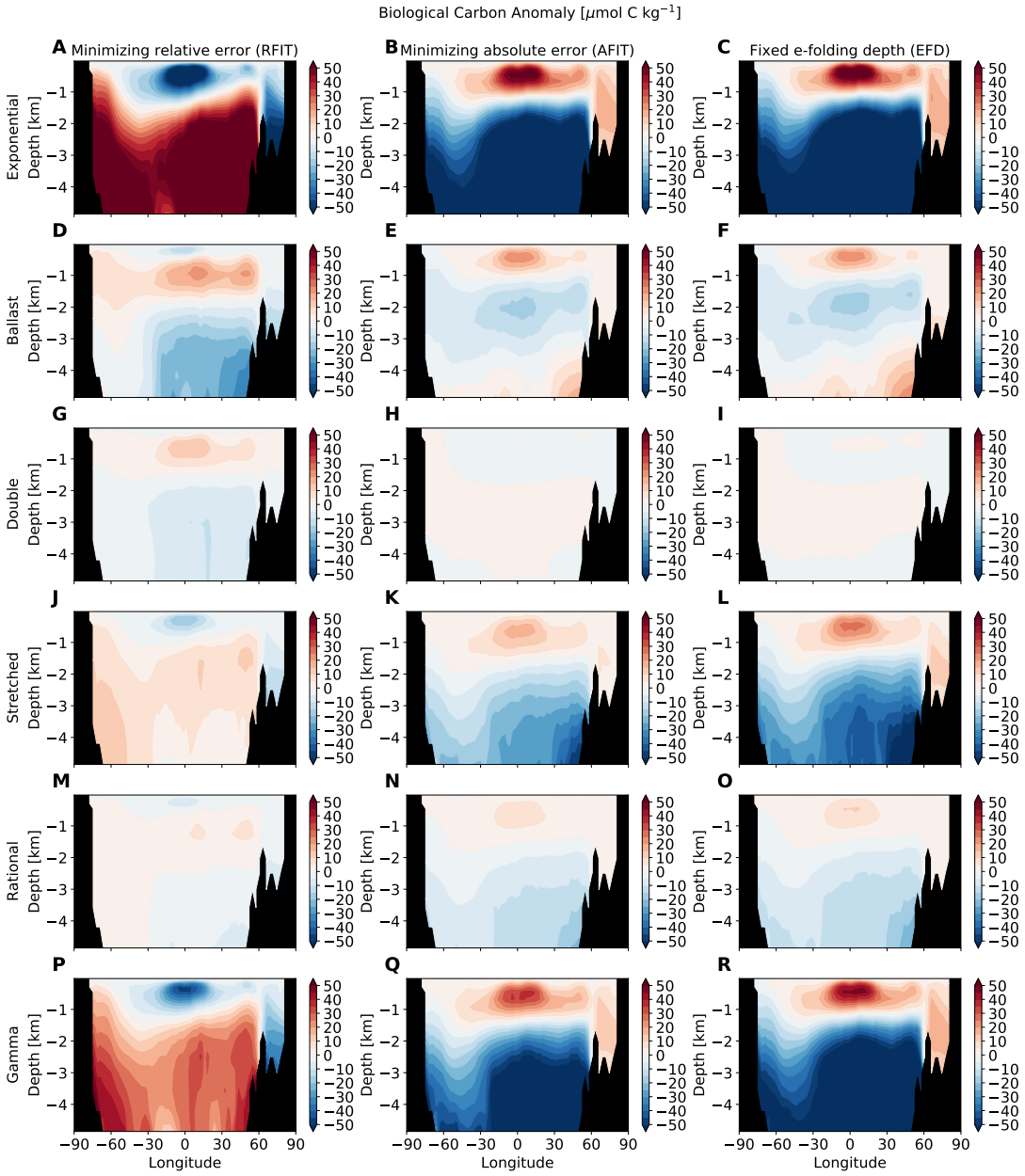

Figure S3. Zonally-averaged biological carbon (C_{bio}) concentrations with respect to the reference power-law curve where $b = 0.84$, for the parameter sets where the relative error of the fit is minimized (RFIT, left column), where the absolute error of the fit is minimized (AFIT, middle column), and where the e-folding depth of remineralization is matched to the 164 m of the control curve (EFD, right column), where (a–c) is the simple exponential profile, (d–f) is the ballast profile, (g–i) is the double exponential profile, (j–l) is the stretched exponential profile, (m–o) is the rational profile, and (p–r) is the gamma profile.

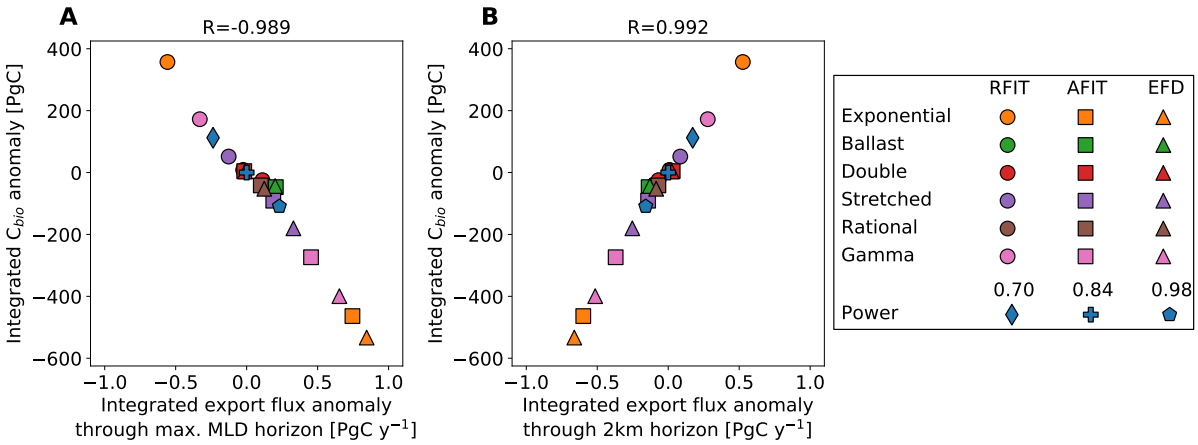

Figure S4. Change in the integrated particle export flux rate [PgC y^{-1}] passing through (a) the horizon of deepest annual mixed layer depth, and (b) the 2 km depth horizon, against integrated biological carbon reservoir anomaly [PgC], both with respect to the power-law curve where $b = 0.84$. Three power-law simulations ($b = 0.84 \pm 0.14$) are indicated by the blue symbols (diamond, cross, and pentagon), circle, square, and triangle symbols indicate that profile coefficients (Eq. S1–S6) were derived by minimizing the relative fit error ("RFIT"), minimizing the absolute fit error ("AFIT"), and fixing the e-folding depth of remineralization ("EFD") to the reference power-law curve. Values are shown in Table S3.

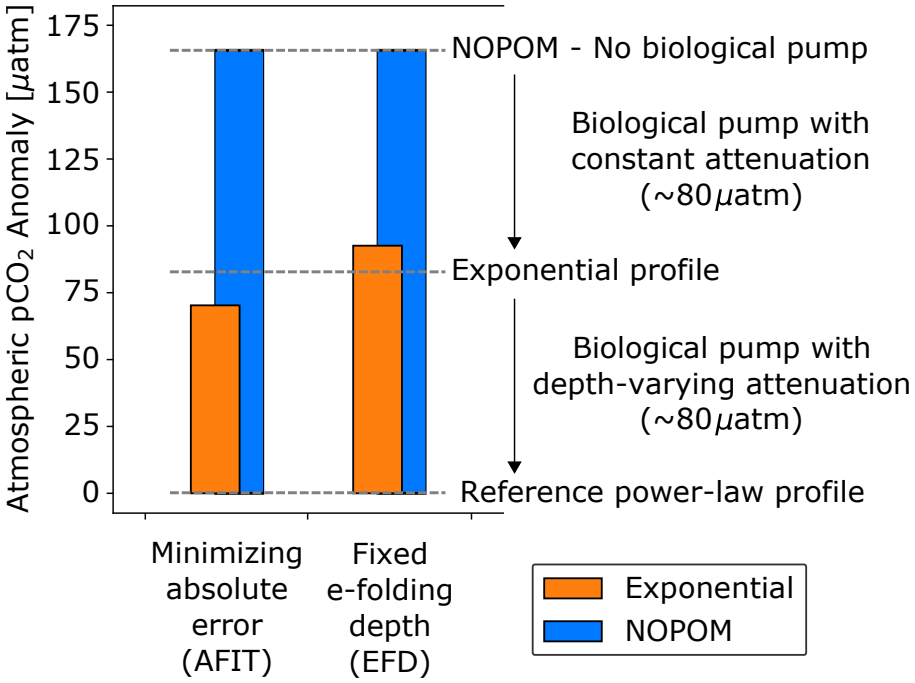

Figure S5. Illustration of the importance of non-linearity in the biological pump remineralization profile. The simple exponential profile, with constant attenuation with depth, leads to significant outgassing of ocean carbon and increases in atmospheric pCO_2 of $\sim 80\mu$atm for AFIT and EFD simulations, despite being statistically fit to the reference power-law. This is roughly half the $\sim 165\mu$atm increase that results from removing the biological pump altogether (NOPOM), highlighting the importance for the air-sea carbon balance, not only of the existence of a biological pump that maintains interior ocean biological carbon stores, but also its non-linearity.

Table S1. Parameter values and fit statistics for remineralization functions (Eq. S1–S6). Each function was matched to the reference power-law (Eq. 1) with exponent $b = 0.84$ by statistically minimizing the relative ("RFIT") or absolute ("AFIT") misfit of the curves, or by matching e-folding remineralization depth scale ("EFD"), Fig. 2b–d. Note different units of coefficients. Goodness of fit is evaluated by $\mathcal{S}$, the Standard Error of Regression (smaller numbers indicate better fit).

Shape	Parameter	Units	RFIT	AFIT	EFD
Exponential	C_e		1.059	1.451	1.548
	ℓ_e	m	871.5	134.2	114.5
	$\mathcal{S}$		1.107	0.0701	0.0700
Ballast	C_b		1.200	1.487	1.530
	ℓ_b	m	226.8	108.6	101.9
	c		0.03111	0.04159	0.04139
	$\mathcal{S}$		0.3838	0.0453	0.0440
Double Exponential	C_{d1}		1.326	1.583	1.522
	ℓ_{d1}	m	124.3	70.38	75.09
	C_{d2}		0.08668	0.1466	0.1492
	ℓ_{d2}	m	2521	1144	1170
	$\mathcal{S}$		0.1559	0.0175	0.0175
Stretched Exponential	C_s		10.88	13.91	15.81
	s		0.7776	0.7526	0.7404
	$\mathcal{S}$		0.2499	0.0260	0.0314
Rational	C_r	m	88.75	69.87	66.61
	a	m	38.75	19.87	16.61
	$\mathcal{S}$		0.1174	0.0112	0.0119
Gamma Function	C_g		0.3214	0.6003	0.7267
	$\ell_{g\,max}$	m	1950	419.6	300.6
	$\mathcal{S}$		0.6272	0.0499	0.0543

Table S2. Supplementary quantities for power-law remineralization simulations with exponents of $b = 0.70$, 0.84, and 0.98, as well as the "NOPOM" simulation where there are no particulate organic matter export fluxes. Reference rates/concentrations are presented for the control power-law curve where $b = 0.84$, while values presented for simulations where $b = 0.70$, 0.98, and NOPOM are anomalies with respect to the control. ΔB_C is the change in globally-integrated rate of net community production, $\Delta \mathrm{E}_{mld}$, $\Delta \mathrm{E}_{1km}$, and $\Delta \mathrm{E}_{2km}$ are the change in areally-integrated particulate organic carbon export flux through the deepest mixed layer depth, 1 km, and 2 km horizons, respectively, ΔC_{bio} is the globally-integrated change in biological carbon (evaluated as dissolved inorganic carbon minus the preformed carbon concentration), and ΔpCO_2^{atm} is the change in atmospheric CO_2 partial pressure.

		Exponent (b)			
		0.70	0.84	0.98	NOPOM
C_p	m^{-1}	1.000	1.000	1.000	
ΔB_C	PgC y^{-1}	-5.231	29.570	5.175	39.65
$\Delta \mathrm{E}_{mld}$	PgC y^{-1}	-0.236	2.349	0.230	-2.349
$\Delta \mathrm{E}_{1km}$	PgC y^{-1}	0.141	1.749	-0.173	-1.749
$\Delta \mathrm{E}_{2km}$	PgC y^{-1}	0.172	0.802	-0.159	-0.802
ΔC_{bio}	PgC	112.32	2363.4	-109.30	-2169
ΔpCO_2^{atm}	μatm	-21.59	269.33	24.77	165.4

Table S3. Supplementary anomalies for alternative remineralization profile simulations. Reference power-law values ($b = 0.84$) are given in Table S2. ΔB_C is the change in globally-integrated net community production rate, $\Delta \mathrm{E}_{mld}$, $\Delta \mathrm{E}_{1km}$, and $\Delta \mathrm{E}_{2km}$ are the change in areally-integrated particulate organic carbon export flux through the deepest mixed layer depth, 1 km, and 2 km horizons, respectively, ΔC_{bio} is the globally-integrated change in biological carbon (evaluated as dissolved inorganic carbon minus the preformed carbon concentration), and ΔpCO_2^{atm} is the change in atmospheric CO_2 partial pressure.

Shape	Parameter	Units	RFIT	AFIT	EFD
Exponential	ΔB_C	PgC y^{-1}	-17.39	7.866	11.01
	$\Delta \mathrm{E}_{mld}$	PgC y^{-1}	-0.558	0.745	0.845
	$\Delta \mathrm{E}_{1km}$	PgC y^{-1}	0.6860	-0.2890	-0.511
	$\Delta \mathrm{E}_{2km}$	PgC y^{-1}	0.5250	-0.5980	-0.662
	ΔC_{bio}	PgC	357.1	-463.9	-533.3
	ΔpCO_2^{atm}	μatm	-62.94	70.28	92.59
Ballast	ΔB_C	PgC y^{-1}	-5.218	2.549	3.108
	$\Delta \mathrm{E}_{mld}$	PgC y^{-1}	0.124	0.205	0.201
	$\Delta \mathrm{E}_{1km}$	PgC y^{-1}	0.3380	-0.244	-0.292
	$\Delta \mathrm{E}_{2km}$	PgC y^{-1}	-0.097	-0.138	-0.130
	ΔC_{bio}	PgC	-38.40	-47.16	-43.58
	ΔpCO_2^{atm}	μatm	-12.39	10.99	12.55
Double Exponential	ΔB_C	PgC y^{-1}	-1.099	-0.2730	-0.553
	$\Delta \mathrm{E}_{mld}$	PgC y^{-1}	0.111	-0.017	-0.011
	$\Delta \mathrm{E}_{1km}$	PgC y^{-1}	0.019	-0.021	-0.010
	$\Delta \mathrm{E}_{2km}$	PgC y^{-1}	-0.069	0.031	0.025
	ΔC_{bio}	PgC	-24.66	4.514	3.255
	ΔpCO_2^{atm}	μatm	-1.761	-1.082	-1.821
Stretched Exponential	ΔB_C	PgC y^{-1}	-5.272	1.226	4.483
	$\Delta \mathrm{E}_{mld}$	PgC y^{-1}	-0.127	0.188	0.329
	$\Delta \mathrm{E}_{1km}$	PgC y^{-1}	0.234	0.056	-0.075
	$\Delta \mathrm{E}_{2km}$	PgC y^{-1}	0.085	-0.142	-0.253
	ΔC_{bio}	PgC	51.61	-90.93	-180.2
	ΔpCO_2^{atm}	μatm	-17.92	10.31	28.60
Rational	ΔB_C	PgC y^{-1}	-2.525	0.892	1.593
	$\Delta \mathrm{E}_{mld}$	PgC y^{-1}	-0.025	0.100	0.124
	$\Delta \mathrm{E}_{1km}$	PgC y^{-1}	0.120	0.000	-0.026
	$\Delta \mathrm{E}_{2km}$	PgC y^{-1}	0.009	-0.069	-0.085
	ΔC_{bio}	PgC	8.479	-41.63	-52.47
	ΔpCO_2^{atm}	μatm	-7.745	5.612	8.583
Gamma Function	ΔB_C	PgC y^{-1}	-11.42	4.023	8.622
	$\Delta \mathrm{E}_{mld}$	PgC y^{-1}	-0.330	0.454	0.653
	$\Delta \mathrm{E}_{1km}$	PgC y^{-1}	0.471	-0.009	-0.282
	$\Delta \mathrm{E}_{2km}$	PgC y^{-1}	0.279	-0.370	-0.514
	ΔC_{bio}	PgC	172.29	-273.74	-399.44
	ΔpCO_2^{atm}	μatm	-40.38	35.70	66.35